Rayleigh-Bénard convection with thermal boundary inhomogeneities

Rayleigh-Bénard convection with thermal boundary inhomogeneities

Francesca Bassani, Davide Poggi, Luca Ridolfi, and Jost von Hardenberg
Department of Environment, Land, and Infrastructure Engineering, Politecnico di Torino, 10129 Torino, Italy

(Received 16 July 2021; revised 18 January 2022; accepted 1 February 2022; published 22 February 2022)

Rayleigh-Bénard convection with nonhomogeneous thermal boundaries (sinusoidal temperature patterns set in-phase at the top and bottom plates) is numerically studied in three- and two-dimensional domains. Two spatial convective scales occur: the one due to the self-organized clustering of plumes—which is known to appear in homogeneous conditions—and the scale induced by the boundary heterogeneities. The latter drives the convection patterning, both in 3D and 2D, when the wavelength of the perturbation is comparable with the self-organized one.

DOI: 10.1103/PhysRevE.105.025108

I. INTRODUCTION

Rayleigh-Bénard (RB) convection [1,2] is one of the simplest, most studied, and paradigmatic examples of thermal convection [3–11]. RB experiments and numerical simulations have traditionally focused on a configuration with thermally homogeneous top and bottom plates. However, boundary inhomogeneities play a crucial role in a number of real cases, e.g., in mantle convection, involving the continental and the oceanic lithosphere [12,13], in sea convection under floating ice [14,15], and in air convection over cities surrounded by rural lands [16]. Some works have investigated heterogeneous temperature boundary conditions (b.c.) on one wall only. Ripesi *et al.* [17] studied alternating thermal insulating and conducting patches on the upper plate in two-dimensions (2D), with a later extension in 3D by Bakhuis *et al.* [18]. Ostilla-Mónico and Amritkar [19] found a relationship between heat transport intensity and the wavelength of adiabatic-conducting stripe pairs. A recent numerical experiment, with inhomogeneities on the lower boundary, simulated a three dimensional cavity [20], demonstrating that nonuniform heating strongly affects the dynamics and structure of large-scale circulation. The effects of nonuniform b.c. on both plates were investigated by Kelly and Pal [21] and Yoo and Moon [22], but for relatively low Rayleigh numbers. All the previous works show that inhomogeneities in thermal boundaries can induce structural changes in RB convection. However, a systematic analysis of nonuniform temperature conditions on both top and bottom boundaries, in the fully turbulent regime, is missing. Are the boundary inhomogeneities able to impose their own scales on the convection? How do these interact with the self-organized large-scale structures emerging from turbulent convection [23–28]? To shed light on this topic, we study top and bottom sinusoidal temperature perturbations in 3D and 2D numerical simulations, exploring a broad range of wavelengths.

II. MODEL AND METHODS

We consider the classical Rayleigh-Bénard configuration, with an incompressible fluid confined between two horizontal, rigid plates, kept at fixed temperatures, with the bottom surface warmer than the top one. Considering the position vector $\mathbf{x} = (x, y, z)$, with z the vertical coordinate, the fields are: velocity $\mathbf{u}(\mathbf{x}, t) = (u, v, w)$, temperature $T(\mathbf{x}, t)$, and pressure $p(\mathbf{x}, t)$. The variables are nondimensionalized through the temperature difference between the plates $\Delta\tilde{T}$, the layer thickness $\tilde{d}$ and the time $\tilde{\tau}_{\text{conv}}$ (the tilde indicates dimensional quantities). The latter represents the convective timescale, given by $\tilde{\tau}_{\text{conv}} = \sqrt{\tilde{d}/(g\alpha\Delta\tilde{T})}$, where g is the gravity acceleration and α the thermal expansion coefficient. Under the Boussinesq approximation [1,9] the equations read

$$\frac{\partial \mathbf{u}}{\partial t} + \mathbf{u}\cdot\nabla\mathbf{u} = -\nabla p + T\hat{\mathbf{z}} + \left(\frac{\sigma}{R}\right)^{1/2}\nabla^2\mathbf{u}, \tag{1}$$

$$\nabla\cdot\mathbf{u} = 0, \tag{2}$$

$$\frac{\partial T}{\partial t} + \mathbf{u}\cdot\nabla T = \frac{1}{(\sigma R)^2}\nabla^2 T, \tag{3}$$

where $\hat{\mathbf{z}}$ is the vertical versor, $\sigma = \nu/\kappa$ is the Prandtl number (kinematic viscosity to thermal diffusivity ratio), and the Rayleigh number $R = g\alpha\Delta\tilde{T}\tilde{d}^3/(\nu\kappa)$. In all simulations, we set $\sigma = 0.71$ (air) and $R = 10^7$.

Periodic b.c. are set in the horizontal directions and z ranges between 0 and 1. The aspect ratio L (the ratio of the planar size of the domain and its thickness $\tilde{d}$) is set to 4π and 8π in 3D and to 32π in 2D. We perform simulations for both no-slip ($\mathbf{u}|_{z=0,1} = 0$) and free-slip ($\partial u/\partial z|_{z=0,1} = \partial v/\partial z|_{z=0,1} = w|_{z=0,1} = 0$) velocity conditions at the top and bottom boundaries.

Thermal b.c. imposed at both plates are $T_b = A\sin(\mathbf{k}\cdot\mathbf{x}) + \overline{T}$ (hereinafter subscript b indicates variables at boundaries), with amplitude $A = 0.25$ and mean $\overline{T} = 0.5$ and $\overline{T} = -0.5$ at the lower and upper boundaries respectively. $\mathbf{k} = (k_x, k_y)$ is the wave number vector of the temperature perturbation, where $k_x = k_y \equiv k_b$. Top and bottom sinusoidal patterns are in phase, so that $\Delta T = 1$ everywhere (in this way, also the local effective R is not altered). To explore different heterogeneity scales, the wavelength $\lambda_b = 2\pi/k_b$ is changed as reported in Table I (the homogeneous case $k_b = 0$ is also investigated).

TABLE I. Wave numbers k_b and wavelengths λ_b of the sinusoidal temperature boundary conditions, for the 2D ($L = 32\pi$) and 3D ($L = 4\pi$ and $L = 8\pi$) domains.

L = 32π (2D)		**L = 4π (3D)**		**L = 8π (3D)**	
k_b	λ_b	k_b	λ_b	k_b	λ_b
0.00625	32π	0.5	4π	0.25	8π
0.125	16π	1	2π		
0.25	8π	1.5	$4\pi/3$		
0.5	4π	2	π		
1	2π	2.5	$4\pi/5$		
1.5	$4\pi/3$	3	$2\pi/3$		
2	π	3.5	$4\pi/7$		
2.5	$4\pi/5$	4	$2\pi/4$		
3	$2\pi/3$				
3.5	$4\pi/7$				
4	$2\pi/4$				
5	$2\pi/5$				
6	$2\pi/6$				

The numerical code employed for integrating Eqs. (1)–(3) is spectral with 4/5 dealiasing in the planar directions and with second-order finite differencing in the vertical, with a nonuniform grid and a third-order fractional step method in time [24,29,30], available on GitHub [31]. We use 193 grid points along z, while the horizontal resolution is $4\pi/512$ in all experiments.

III. RESULTS

In a homogeneous three-dimensional RB configuration, plumes are known to organize themselves into clusters [24]. After an initial transient, the aggregation among horizontal large-scale structures reaches a statistically stationary state and the clustering is evident, as shown in Figs. 1(a_{1-3}) for the no-slip cases (see also Figs. S1(a_{1-3}) of the Supplemental Material [32], for free-slip conditions). Figure 1(a_1), showing the temperature at midplane, clearly reveals the clustering of thermals of the same sign [25]. The snapshots of the vertical velocities w and the vertical heat fluxes in Figs. 1(a_{2-3})—calculated as the product between w and the temperature anomalies T'—show that intense w are associated with high positive values of wT' where warm (cold) structures are ascending (descending).

The clustering phenomenon is further highlighted by the horizontal power spectrum $E(k)$ of the kinetic energy $(u^2 + v^2 + w^2)/2$ [see the asterisks in Figs. 2(a)–2(c)]. The spectrum associated with the homogeneous case $k_b = 0$ peaks at the horizontal wave number $k_{so} \simeq 1$ (see the red asterisk), corresponding to wavelength $\lambda_{so} \simeq 2\pi$: this is the typical size of the large-scale patterns [25] emerging in Fig. 1(a_1). Hereinafter, we refer to E_{so} for the energy spectrum peak value at the self-organized scale k_{so}. In the following, we show that the clustering-induced structures occur not only when the thermal b.c. are uniform, but also with inhomogeneities. In particular, we explore (i) if nonhomogeneous thermal boundary conditions are able to force novel convective structures and (ii) their interaction with the self-organized clusters already observed in the homogeneous case.

We begin with the two 3D cases where the wavelengths of the boundary inhomogeneities are comparable to the domain size: $\lambda_b = 8\pi$ ($k_b = 0.25$) in $L = 8\pi$ and $\lambda_b = 4\pi$ ($k_b = 0.5$) in $L = 4\pi$. The temperature fields reported in Figs. 1(b_1-c_1), would seem to show that in both cases the imposed boundary anomalies affect the convection pattern, by localizing the structures in preferred spots of the domain, in phase with the boundary inhomogeneities. However, temperature snapshots alone could be misleading, since the presence of hotter or colder zones does not necessarily indicate vertical motion of the fluid. Instead, looking at the vertical velocity panels, when $k_b = 0.5$ the boundary perturbations do effectively have an impact on w [Fig. 1(c_2)]: the convective vertical motions exhibit the same (in phase) large-scale pattern of boundary heterogeneities. On the contrary, forcing at a significantly larger scale with $\lambda_b = 8\pi$ ($k_b = 0.25$) does not have a significant impact on the scale of horizontal structures, which exhibit a clustering scale close to $\lambda_{so} = 2\pi$. In fact, in this case, w [Fig. 1(b_2)] is clearly distributed over the 8π domain similarly to the uniform case: notice how panel b_2 resembles the tessellation of four panels like a_2, where $k_b = 0$. This is confirmed also by the power spectrum $W(k)$ of the vertical velocity component, which exhibits a lower peak at $k = 0.25$ than at the self-organized scale $k = 1$ (see Figs. S1(e) and S1(f) in the Supplemental Material [32]). This result is also supported by the heat fluxes [Figs. 1(b_3-c_3)] and by the mean Pearson cross-correlation coefficient between the temperature and the vertical velocity, which is $r(T, w) \simeq 0.04$ for $k_b = 0.25$, while it is $\simeq 0.35$ for $k_b = 0.5$. It emerges that when $k_b \ll k_{so}$, the boundary forcing is unable to impose its own scale and the system is organized according to the self-organized scale $k_{so} \simeq 1$ as in the homogeneous case.

The scenario does not change when considering a forcing wave number k_b greater than the self-organized wave number k_{so}. Also in this case, the scale of the b.c. is no longer perceived and the convection is not significantly affected by the boundary inhomogeneities. The structures aggregate randomly over the domain and exhibit only the typical self-organized scale $\lambda_{so} \simeq 2\pi$. Figures 1(d_{1-3}) illustrates an example corresponding to the case $k_b = 3$, but the same behavior is found for any $k_b \geqslant 2$.

All the previous snapshots provide a qualitative overview of the problem. To quantitatively identify when the boundary conditions are able to influence the convective process, the horizontal power spectrum $E_0(k)$ of the homogeneous case is compared with the spectra $E_b(k)$ for the cases $k_b = 0.25$, $k_b = 0.5$, and $k_b = 3$ in Figs. 2(a)–2(c); all the other cases are reported in Figs. S2 and S3 of the Supplemental Material [32]. In particular, we focus on (i) the maximum spectral density $E_{so} \equiv E_0(k_{so})$ occurring in the homogeneous case at the scale of clustering $k_{so} = 1$, and (ii) the spectral density $E_{ex} \equiv E_b(k_b)$, associated with the externally imposed scale k_b (the subscript "ex" recalls that this scale is exogenous). In Figs. 2(a)–2(c), the former is marked with a red asterisk and the latter with a black circle. An additional red circle indicates the value $E_{b,so} \equiv E_b(k_{so})$ of the spectrum corresponding to the nonuniform cases at the self-organized wave number.

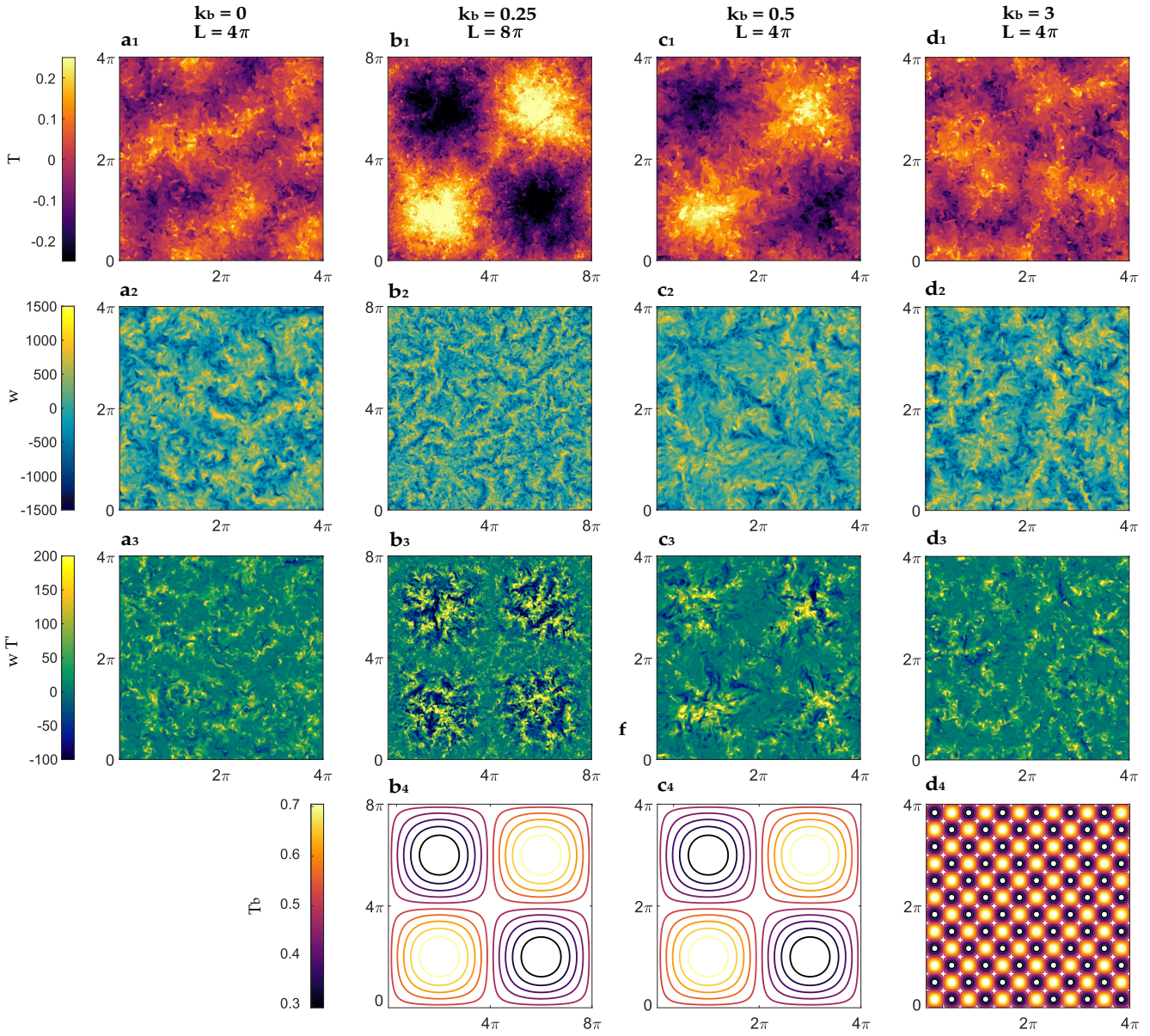

FIG. 1. 3D simulations: snapshots at $z = 1/2$ and $\tau_{\text{conv}} = 180$ of the temperature perturbations T (first row, subscript 1), vertical velocity field w (subscript 2), and vertical flux wT' (subscript 3), under no-slip conditions. Panels $\mathbf{b_{1-3}}$ refer to the domain $L = 8\pi$, while panels $\mathbf{a_{1-3}}$, $\mathbf{c_{1-3}}$, and $\mathbf{d_{1-3}}$ correspond to $L = 4\pi$. Panels $\mathbf{b_4}$, $\mathbf{c_4}$, and $\mathbf{d_4}$ provide a visualization (with isotherms) of the boundary conditions T_b at the bottom plate.

The interplay between the self-organized and the exogenous scales given by the ratio $E_{\text{ex}}/E_{\text{so}}$ is shown in Fig. 3 (black line). A ratio greater than 1 indicates that the thermal b.c. strongly influence the convection patterning, leading to a spectral peak at the forcing scale which is higher that the self-organized one in the homogeneous case. In this case, the external inhomogeneities reinforce the self-organized arrangement of the structures in the domain and the ascending (descending) plumes tend to organize themselves and to develop where the b.c. have positive (negative) values of temperature. Figure 3 shows that this occurs for $k_b = 0.5, 1, 1.5$ under no-slip conditions and for $k_b = 0.5$ in free-slip, all values that are close to the scale $k_{\text{so}} = 1$.

The extent by which the external forcing is capable of imposing its own scale on the flow can be seen considering the ratio between the spectral values at the self-organized scale for the nonhomogeneous and homogeneous cases $E_{b,\text{so}}/E_{\text{so}}$ (compare the red and black lines in Fig. 3). When this ratio is below or equal to $E_{\text{ex}}/E_{\text{so}}$ the boundary anomalies are imposing their scale on the flow, while when $E_{b,\text{so}}/E_{\text{so}}$ prevails, the exogenous scale becomes negligible with respect to the self-organized one, suggesting clustering as in the homogeneous case.

Figure 3 therefore shows that the nonuniform boundaries are able to induce convective structures of size comparable to the perturbation wavelength, and to localize them, only

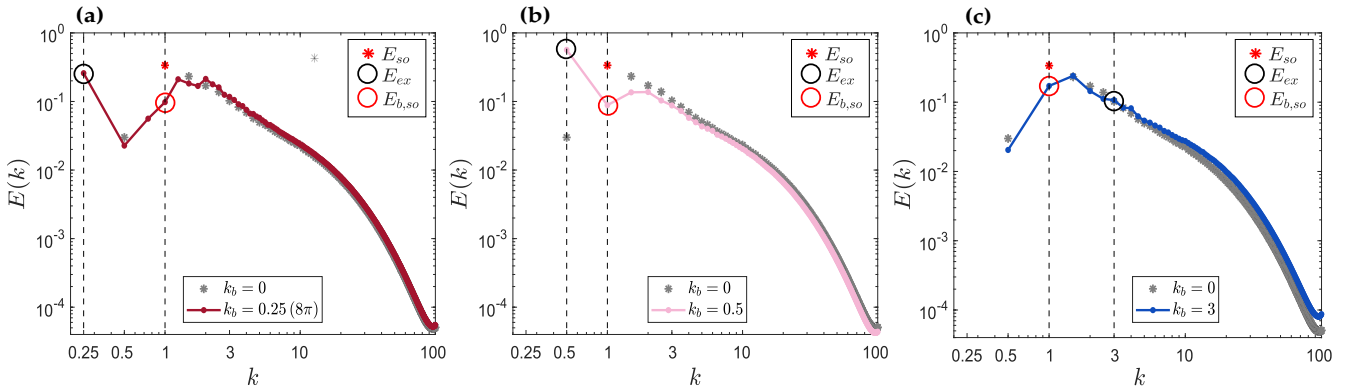

FIG. 2. 3D simulations: horizontal power spectra (normalized to unit variance and averaged over the vertical fluid column and times $\tau_{\rm conv} = 180 \div 220$) of the no-slip kinetic energy $E(k)$, plotted as functions of the horizontal wave number k for the cases $k_b = 0.25$ (a), $k_b = 0.5$ (b), and $k_b = 3$ (c). The spectrum for the homogeneous case ($k_b = 0$) is shown with gray asterisks for reference. The spectral peak $E_{\rm so}$ in the homogeneous case is marked with a red asterisk, while the spectral values (in the heterogeneous cases) corresponding to the exogenous scale ($E_{\rm ex}$) and self-organized scale ($E_{b,\rm so}$) are highlighted with a black and red circle, respectively.

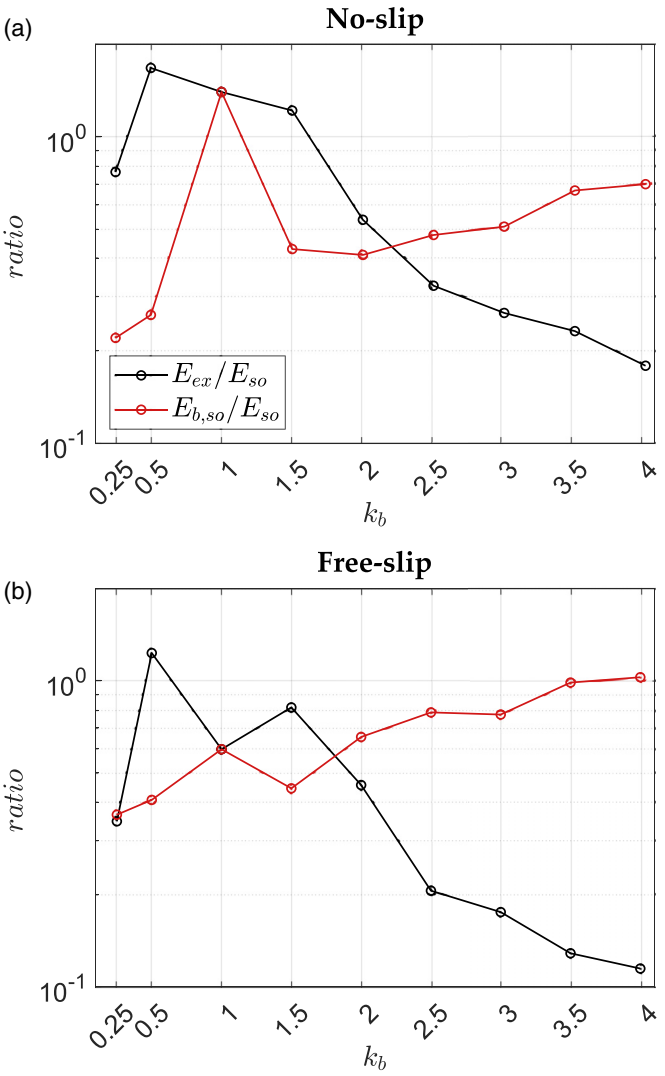

FIG. 3. 3D simulations: $E_{\rm ex}/E_{\rm so}$ (black line) and $E_{b,\rm so}/E_{\rm so}$ (red line), as functions of the b.c. wave numbers k_b, for the no-slip (a) and free-slip (b) cases.

when the scale of the forcing is sufficiently close to the self-organized one. Otherwise, the clustering of structures occurs at the self-organized scale.

These findings are confirmed also by the integral length scale of the convection $\lambda_I = \int [E(k)/k]\,dk / \int E(k)\,dk$, which is a quantitative measure of the clustering scale based on the depth-averaged kinetic energy spectra [24,25]. The mean $\overline{\lambda_I}$, averaged from $\tau_{\rm conv} = 40$ (so that the initial transient phase is neglected) to $\tau_{\rm conv} = 220$ (end of the simulations) for each thermal heterogeneity, is shown in Fig. 4. Both under no-slip and free-slip boundary conditions, we observe substantially higher $\overline{\lambda_I}$ for wave numbers k_b close to $k_{\rm so}$, because of their capability to impose a new, larger, exogenous scale on the convection, overcoming the self-organized one; instead, the remaining cases exhibit a scale similar to that of the homogeneous case.

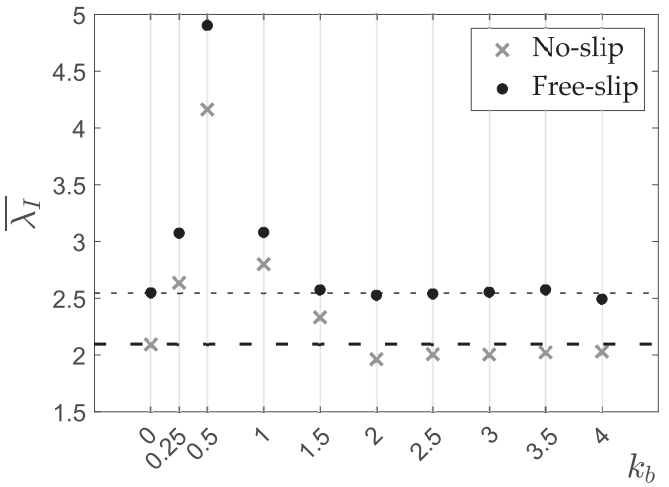

FIG. 4. Time-averaged ($\tau_{\rm conv} = 40 \div 220$) integral scale $\overline{\lambda_I}$ of the 3D simulations. The horizontal dashed lines refer to $\overline{\lambda_I}$ when $k_b = 0$, for the no-slip (thick line) and the free-slip (thin line) cases.

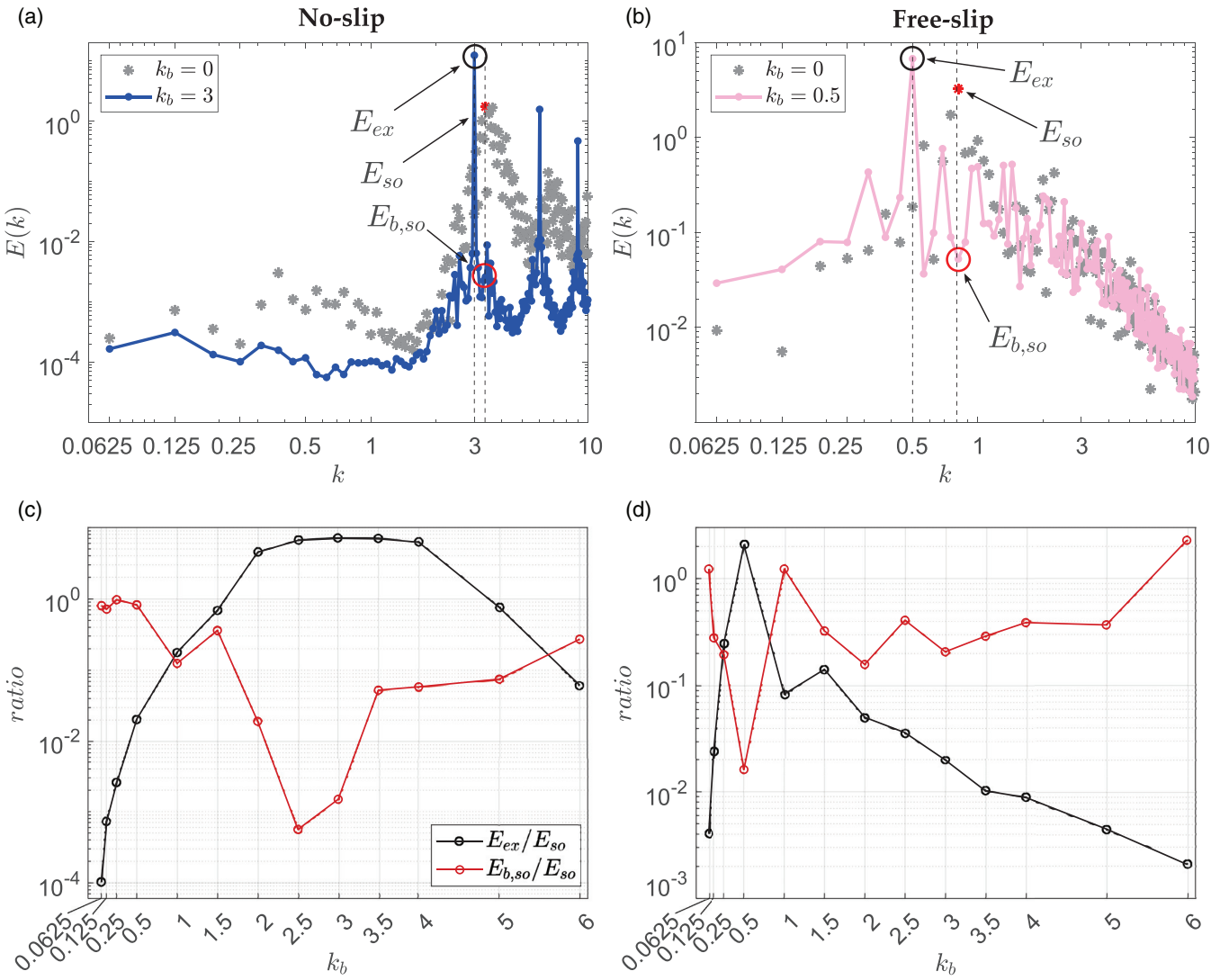

FIG. 5. Low-k part of the kinetic energy spectra (averaged over the vertical fluid column and times $\tau_{\rm conv} = 180 \div 220$) of the 2D no-slip case $k_b = 3$ (a) and 2D free-slip $k_b = 0.5$ (b). The spectrum for the homogeneous case $k_b = 0$ is shown with gray asterisks for reference. The values $E_{\rm so}$, $E_{\rm ex}$ and $E_{b,\rm so}$ are marked with a red asterisk, a black and a red circle, respectively. Panels c and d show the two ratios $E_{\rm ex}/E_{\rm so}$ (black line) and $E_{b,\rm so}/E_{\rm so}$ (red line) as a function of the b.c. wave numbers k_b, for all the no-slip (c) and free-slip (d) cases.

To verify further the capability of nonuniform boundaries with k_b close to $k_{\rm so}$ to induce their own scale on the convection, we consider a two-dimensional systems characterized by an aspect ratio equal to 32π (Table I). This choice allows us the exploration of k_b down to 0.0625, overcoming the limit of small 3D domain dimensions. Moreover, we extend the analysis to wave numbers $k_b = 5$ and 6, to confirm that high-frequency b.c. have no evident effect on the convection.

In terms of 2D patterning, we find a behavior similar to that observed in the 3D case. In fact, three elements emerge. First, the self-organized scale occurs both under uniform and nonuniform boundaries. Second, nonhomogeneous boundary temperatures, having intermediate values of k_b, are able to force the formation of structures around such heterogeneities, exhibiting scales at the b.c. wavelength. Finally, the impact of external thermal perturbations weakens with growing boundary wave number, resulting in a behavior of the system dominated by the self-organized scales, also observed in the homogeneous case $k_b = 0$. Representative vertical sections of the temperature, velocity and flux fields proving these findings are reported in Fig. S5 of the Supplemental Material [32].

Figures 5(a) and 5(b) show two of the most representative spectra $E(k)$ obtained for the two-dimensional simulations, where the exogenous peak $E_{\rm ex}$ largely overcomes the self-organized one. All the other spectra are shown in Fig. S6 and S7 of the Supplemental Material [32]. Having confirmed the existence of the self-organized structures also in 2D, the interaction between the self-organized and the exogenous scales is highlighted by the metric $E_{\rm ex}/E_{\rm so}$, shown in Figs. 5(c) and 5(d). A ratio $E_{\rm ex}/E_{\rm so} > 1$—for which the b.c. affect the convection patterning—here occurs for k_b between 2 and 4 under no-slip conditions and for $k_b = 0.5$ in free-slip. Such pattern-inducing values of k_b are around the self-organized scales $k_{\rm so} \simeq 3$ [no-slip, red asterisk in Fig. 5(a)] and $\simeq 0.8$ [free-slip, Fig. 5(b)]. Otherwise, the clustering occurs at the

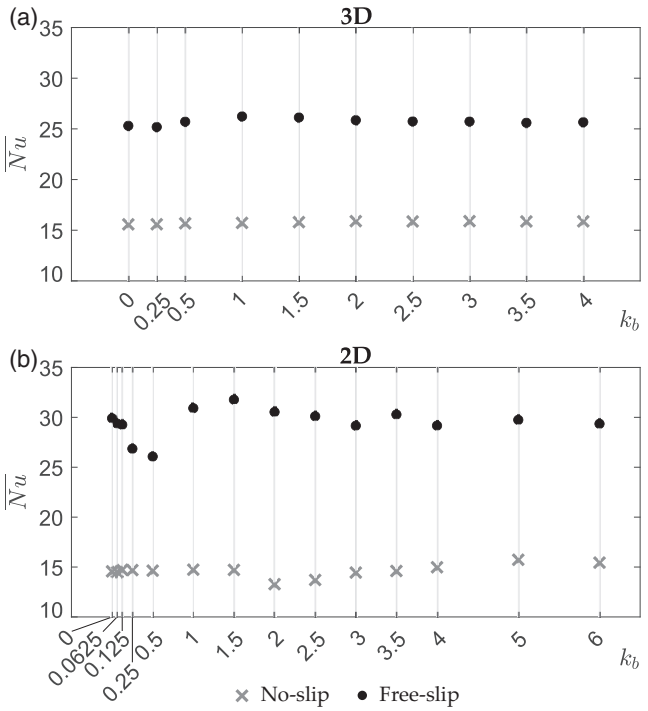

FIG. 6. Time-averaged ($\tau_{\text{conv}} = 40 \div 220$) Nusselt number $\overline{\text{Nu}}$ of each analyzed case, for the 3D (a) and 2D (b) simulations. The no-slip cases are marked by gray crosses, while the free-slip cases by black dots.

self-organized scale, as highlighted by a greater ratio $E_{b,\text{so}}/E_{\text{so}}$ than $E_{\text{ex}}/E_{\text{so}}$ [Figs. 5(c)–5(d)].

The 2D cases confirm that—as already observed in 3D—values of the imposed wave number k_b significantly greater or smaller than k_{so}, produces no relevant impact on the convection: the only observed scale remains the self-organized one. The exogenous scale prevails over the self-organized one only when the nonhomogeneous boundaries are characterized by a wave number k_b close to k_{so}.

The spectra allow us to capture another aspect: under no-slip conditions the peak E_{so} occurs around the horizontal wave number $k = 3$ [red asterisk in Fig. 5(a)], while in free-slip conditions the self-organized peak occurs at $k \simeq 0.8$ [Fig. 5(b)]. This is in line with the results discussed in Refs. [33,34] which analyzed the relationship between roll number, Rayleigh and Prandtl number for stable 2D RB solutions, showing that in large aspect ratio domains multiple stable states are possible. This also suggests that, at least in 2D RB convection, a narrow range of possible stable k_{so} values is possible and we expect that it is in this range that the k_b imposed by the boundary conditions will have a greater impact on the flow. Further future exploration of a broader range of σ and R values could be useful to explore this point.

Another relevant issue concerns the effects produced by the thermal heterogeneities on the Nusselt number Nu. Figure 6 shows the time-averaged $\overline{\text{Nu}}$ as a function of the imposed k_b: both in 3D and in 2D [Figs. 6(a) and 6(b), respectively] the convection is stronger in free-slip than in no-slip conditions. However, the flow topology seems not consistently affected by the temperature boundary anomalies, since their $\overline{\text{Nu}}$ is very close to that found under homogeneous conditions ($k_b = 0$). The only exception emerges for the 2D free-slip forcing at $k_b = 0.25$ and 0.5, for which $\overline{\text{Nu}}$ is slightly lower than its mean value. This is consistent with the spectral peak at a lower wave number $k = 0.5$ in the $k_b = 0.5$ case (see Fig. 5(b) and Fig. S2 in Ref. [32] for comparison) and the link between larger aspect ratio of large-scale rolls and lower Nusselt number discussed in Ref. [33].

IV. CONCLUSIONS

We have found that thermal boundary inhomogeneities applied in-phase on both plates of a Rayleigh-Bénard configuration, can play a crucial role. Our work demonstrates that self-organized structures, or thermal superstructures [27] (up to now observed under uniform conditions only), are not inhibited by the presence of exogenous heterogeneities on the boundaries. Our main result is that the introduction of nonhomogeneous boundaries produces another convective scale in the system, which determines the position and the size of thermal structures, only when the scale of the perturbation is close to the scale of the self-organized clustering. If they are not comparable, the effects produced by the boundaries on the convection are negligible, resulting in a behavior similar to that obtained under homogeneous conditions. The setup considered in this work, introducing a horizontal temperature modulation on the boundaries, is also connected to the so-called problem of horizontal convection [35], where a horizontal temperature gradient drives convection. This may justify the appearance of horizontal winds at the scale of the boundary perturbation, as reported above for the 3D case $k_b = 0.25$, but this topic deserves further future investigation.

ACKNOWLEDGMENTS

F.B. and L.R. acknowledge financial support from the Regional Agency for the Protection of the Environment of Piedmont Region (ARPA Piemonte). Part of the computational resources were provided by HPC@POLITO [36].

[1] L. Rayleigh, LIX. On convection currents in a horizontal layer of fluid, when the higher temperature is on the under side, Philos. Mag. **32**, 529 (1916).

[2] D. Avsec, Tourbillons thermoconvectifs dans l'air, Ph.D. thesis, Université de Paris 1939.

[3] E. D. Siggia, High Rayleigh number convection, Annu. Rev. Fluid Mech. **26**, 137 (1994).

[4] A. V. Getling and E. A. Spiegel, Rayleigh-Bénard convection: Structures and dynamics, Phys. Today **52**(9), 59 (1999).

[5] E. Bodenschatz, W. Pesch, and G. Ahlers, Recent developments in Rayleigh-Bénard convection, Annu. Rev. Fluid Mech. **32**, 709 (2000).

[6] G. Ahlers, S. Grossmann, and D. Lohse, Heat transfer and large scale dynamics in turbulent Rayleigh-Bénard convection, Rev. Mod. Phys. **81**, 503 (2009).

[7] D. Lohse and K.-Q. Xia, Small-scale properties of turbulent Rayleigh-Bénard convection, Annu. Rev. Fluid Mech. **42**, 335 (2010).

[8] F. Chillà and J. Schumacher, New perspectives in turbulent Rayleigh-Bénard convection, Eur. Phys. J. E **35**, 1 (2012).

[9] S. Chandrasekhar, *Hydrodynamic and Hydromagnetic Stability* (Courier Corporation, North Chelmsford, MA, 2013).

[10] D. Goluskin, *Internally Heated Convection and Rayleigh-Bénard Convection* (Springer, Berlin, 2016).

[11] O. Shishkina, Rayleigh-Bénard convection: The container shape matters, Phys. Rev. Fluids **6**, 090502 (2021).

[12] C. Jaupart and J.-C. Mareschal, 6.05—Heat flow and thermal structure of the lithosphere, in *Treatise on Geophysics*, 2nd ed., edited by G. Schubert (Elsevier, Oxford, 2015), pp. 217–253.

[13] F. Wang, S.-D. Huang, and K.-Q. Xia, Thermal convection with mixed thermal boundary conditions: Effects of insulating lids at the top, J. Fluid Mech. **817**, R1 (2017).

[14] G. A. Maykut, Large-scale heat exchange and ice production in the central Arctic, J. Geophys. Res. **87**, 7971 (1982).

[15] Z. Wang, E. Calzavarini, C. Sun, and F. Toschi, How the growth of ice depends on the fluid dynamics underneath, Proc. Natl. Acad. Sci. USA **118**, e2012870118 (2021).

[16] L. Zhao, X. Lee, R. B. Smith, and K. Oleson, Strong contributions of local background climate to urban heat islands, Nature (London) **511**, 216 (2014).

[17] P. Ripesi, L. Biferale, M. Sbragaglia, and A. Wirth, Natural convection with mixed insulating and conducting boundary conditions: Low- and high-Rayleigh-number regimes, J. Fluid Mech. **742**, 636 (2014).

[18] D. Bakhuis, R. Ostilla-Mónico, E. P. Van Der Poel, R. Verzicco, and D. Lohse, Mixed insulating and conducting thermal boundary conditions in Rayleigh–Bénard convection, J. Fluid Mech. **835**, 491 (2018).

[19] R. Ostilla-Mónico and A. Amritkar, Regime crossover in Rayleigh-Bénard convection with mixed boundary conditions, J. Fluid Mech. **903**, 39 (2020).

[20] A. Vasiliev and A. Sukhanovskii, Turbulent convection in a cube with mixed thermal boundary conditions: Low Rayleigh number regime, Int. J. Heat Mass Transf. **174**, 121290 (2021).

[21] R. Kelly and D. Pal, Thermal convection with spatially periodic boundary conditions: Resonant wavelength excitation, J. Fluid Mech. **86**, 433 (1978).

[22] J.-S. Yoo and M.-U. Kim, Two-dimensional convection in a horizontal fluid layer with spatially periodic boundary temperatures, Fluid Dyn. Res. **7**, 181 (1991).

[23] T. Hartlep, A. Tilgner, and F. H. Busse, Large Scale Structures in Rayleigh-Bénard Convection at High Rayleigh Numbers, Phys. Rev. Lett. **91**, 064501 (2003).

[24] A. Parodi, J. von Hardenberg, G. Passoni, A. Provenzale, and E. A. Spiegel, Clustering of Plumes in Turbulent Convection, Phys. Rev. Lett. **92**, 194503 (2004).

[25] J. von Hardenberg, A. Parodi, G. Passoni, A. Provenzale, and E. Spiegel, Large-scale patterns in Rayleigh-Bénard convection, Phys. Lett. A **372**, 2223 (2008).

[26] A. Pandey, J. D. Scheel, and J. Schumacher, Turbulent superstructures in Rayleigh-Bénard convection, Nat. Commun. **9**, 1 (2018).

[27] R. J. A. M. Stevens, A. Blass, X. Zhu, R. Verzicco, and D. Lohse, Turbulent thermal superstructures in Rayleigh-Bénard convection, Phys. Rev. Fluids **3**, 041501(R) (2018).

[28] D. Krug, D. Lohse, and R. Stevens, Coherence of temperature and velocity superstructures in turbulent Rayleigh-Bénard flow, J. Fluid Mech. **887**, 2A2 (2020).

[29] G. Passoni, G. Alfonsi, and M. Galbiati, Analysis of hybrid algorithms for the Navier–Stokes equations with respect to hydrodynamic stability theory, Int. J. Numer. Methods Fluids **38**, 1069 (2002).

[30] J. von Hardenberg, D. Goluskin, A. Provenzale, and E. A. Spiegel, Generation of Large-Scale Winds in Horizontally Anisotropic Convection, Phys. Rev. Lett. **115**, 134501 (2015).

[31] J. von Hardenberg, RBsolve: Pseudospectral Rayleigh-Bénard solver, https://doi.org/10.5281/zenodo.6088505.

[32] See Supplemental Material at http://link.aps.org/supplemental/10.1103/PhysRevE.105.025108 for Figs. S1–S8. Figure S1 shows the horizontal sections of temperature perturbations, vertical velocity field, and vertical heat flux under free-slip conditions (3D domain). Fig. S1 also reports the spectra of the vertical velocity field, both under free- and no-slip conditions in 3D. Figures S2 and S3 show the horizontal power spectra of the kinetic energy for every case of the 3D no-slip and free-slip b.c., respectively. Figure S4 shows the near-boundary sections of the horizontal velocity fields for the 3D cases in the domain $L = 8\pi$. Figure S5 reports the vertical sections of temperature, velocity and flux fields in 2D, under both no- and free-slip conditions. Figures S6 and S7 show the horizontal power spectra of the kinetic energy for all cases analyzed in 2D. Figure S8 shows the time-series of the Nusselt number for 3D and 2D simulations.

[33] Q. Wang, K. L. Chong, R. J. Stevens, R. Verzicco, and D. Lohse, From zonal flow to convection rolls in Rayleigh–Bénard convection with free-slip plates, J. Fluid Mech. **905**, 21 (2020).

[34] Q. Wang, R. Verzicco, D. Lohse, and O. Shishkina, Multiple States in Turbulent Large-Aspect-Ratio Thermal Convection: What Determines the Number of Convection Rolls? Phys. Rev. Lett. **125**, 074501 (2020).

[35] G. O. Hughes and R. W. Griffiths, Horizontal convection, Annu. Rev. Fluid Mech. **40**, 185 (2008).

[36] HPC@POLITO, a project of Academic Computing within the Department of Control and Computer Engineering at the Politecnico di Torino, http://www.hpc.polito.it.